PHYSICAL REVIEW B VOLUME 59, NUMBER 11 15 MARCH 1999-I

Energy spectrum and topology evolution of the Fermi surface of two-dimensional holes in GaAs/Al$_{0.5}$Ga$_{0.5}$As heterostructures under uniaxial compression: Theory and experiment

K. I. Kolokolov, A. M. Savin, S. D. Beneslavski, and N. Ya. Minina
Physics Faculty, Moscow State University, 119899 Moscow, Russia

O. P. Hansen
Niels Bohr Institute, University of Copenhagen, Copenhagen 2100, Denmark

(Received 13 July 1998)

Valence-band structure and transport properties of two-dimensional holes in *p*-type GaAs/Al$_{0.5}$Ga$_{0.5}$As asymmetric quantum wells under uniaxial compression have been investigated both theoretically and experimentally. The Luttinger-Kohn Hamiltonian with strain terms was self-consistently solved by using the finite-difference $\mathbf{k}\cdot\mathbf{p}$ method. The Fermi surface was found to become strongly anisotropic under the application of in-plane uniaxial compression, and the differences between the hole concentrations in the ground-state splitted subband and between the corresponding effective masses to decrease. The electrical resistance becomes strongly anisotropic under applied compression, decreasing in the direction parallel to the compression and increasing in the perpendicular direction. [S0163-1829(99)00408-7]

I. INTRODUCTION

The absence of inversion symmetry of the confining potential in single *p*-type GaAs/Al$_x$Ga$_{1-x}$As heterostructures leads to a splitting of the hole subbands. The qualitative difference between the properties of two-dimensional (2D) holes in symmetric and asymmetric GaAs/Al$_x$Ga$_{1-x}$As quantum wells was detected experimentally[1,2] and it was ascribed to the different symmetry of the confining potential. Later theoretical calculations confirmed a considerable band splitting and a complicated nonparabolic dispersion law in *p*-type GaAs/Al$_x$Ga$_{1-x}$As heterostructures with triangular quantum wells.[3–5] Hole effective masses in the system were found to have a significant dependence on magnetic field.[1,4]

Influence of strain is very important for the band structure of heterostructures and for their application in real devices, as the lattice mismatch unavoidably causes a biaxial strain. This kind of strain considerably modifies the band structure of 2D hole systems. In *p*-type In$_x$Ga$_{1-x}$As/In$_x$Ga$_{1-x}$As$_y$P$_{1-y}$ high biaxial strain leads to large shifts of the hole subbands,[6] the light-hole subband becoming the upper one at a definite biaxial tension. The biaxial strain affects the value of the splitting in the system,[6,7] and compressive and tensile strains can strongly increase or suppress existing splitting.[6] The influence of uniaxial stress on the valence-band structure was also studied, but only for the case of square wells.[8–10] Contrary to the intensive theoretical and experimental investigations of *p*-type heterostructures under biaxial deformation, less attention was paid to the influence of uniaxial stress, probably due to its more ''artificial'' nature. In the present paper, we report on (i) the results of numerical calculations of a single *p*-type [001]GaAs/Al$_{0.5}$Ga$_{0.5}$As heterostructure valence-band structure under external uniaxial compression applied along the [110] and [100] directions (Sec. II), (ii) the experimental data obtained on such a heterostructure under [110] and [$\overline{1}10$] uniaxial compressions up to 5 kbar (Sec. III), and (iii) our analysis of the experimental and theoretical results (Sec. IV).

II. THEORY

The 4×4 Luttinger-Kohn Hamiltonian[11] describing the band structure of the upper four valence bands around Γ_8 was used in this work, the split-off subband at Γ_7, lying 340 meV below the top of the valence band, was neglected. All calculations were performed in the Hartree approximation, many-body effects and terms linear in k were neglected.

In the presence of uniaxial stress the Hamiltonian is modified according to the Bir-Pikus strain Hamiltonian description[12]

$$H=H_{lk}+H_{\epsilon}, \tag{1}$$

where H_{lk} is the Luttinger-Kohn Hamiltonian for the valence band and H_{ϵ} is the strain Hamiltonian

$$H_{\epsilon}=-a_v(\varepsilon_{xx}+\varepsilon_{yy}+\varepsilon_{zz})-b\left[\left(J_x^2-\frac{J^2}{3}\right)\varepsilon_{xx}+\text{c.p.}\right]$$
$$-\frac{2}{\sqrt{3}}d[(J_x,J_y)\varepsilon_{xy}+\text{c.p.}]. \tag{2}$$

Here, a_v, b, and d are deformation potentials for the valence band, ε_{ij} are components of the strain tensor, and J_i are the angular momentum matrices corresponding to a $\frac{3}{2}$ state. The total Hamiltonian is then written as

$$H=\begin{bmatrix} P+Q & R & -S & 0 \\ R^* & P-Q & 0 & S \\ -S^* & 0 & P-Q & R \\ 0 & S^* & R^* & P+Q \end{bmatrix}, \tag{3}$$

where

$$P\pm Q=-\frac{\hbar^2}{2m_e}[(\gamma_1\pm\gamma_2)(k_x^2+k_y^2)+(\gamma_1\mp 2\gamma_2)k_z^2] -a_v(\varepsilon_{xx}+\varepsilon_{yy}+\varepsilon_{zz})\mp b\left[\varepsilon_{zz}-\frac{1}{2}(\varepsilon_{xx}+\varepsilon_{yy})\right], \tag{4}$$

$$R=-\frac{\hbar^2\sqrt{3}}{2m_e}[\gamma_2(k_x^2-k_y^2)-2i\gamma_3k_xk_y] -\frac{\sqrt{3}}{2}b(\varepsilon_{yy}-\varepsilon_{xx})-id\varepsilon_{xy}, \tag{5}$$

$$S=-i\frac{\hbar^2}{m_e}\gamma_3\sqrt{3}(k_x-ik_y)k_z+d(\varepsilon_{yz}+i\varepsilon_{zx}), \tag{6}$$

where m_e is the free-electron mass, γ_i are the Luttinger constants. This 4×4 matrix can be reduced to two 2×2 matrices by using the transformation[5,9]

$$U=\frac{1}{\sqrt{2}}\begin{bmatrix} e^{-i\varphi} & 0 & 0 & -e^{i\varphi}\\ 0 & e^{-i\eta} & -e^{i\eta} & 0\\ 0 & e^{-i\eta} & e^{i\eta} & 0\\ e^{-i\varphi} & 0 & 0 & e^{i\varphi}\end{bmatrix} \tag{7}$$

with

$$\varphi=\frac{\pi}{4}+\frac{1}{2}(\alpha+\beta),\qquad \eta=\frac{\pi}{4}-\frac{1}{2}(\alpha-\beta), \tag{8}$$

where

$$\tan(\alpha)=-\frac{\dfrac{\hbar^2}{m_e}\sqrt{3}\gamma_3k_xk_y-d\varepsilon_{xy}}{\dfrac{\hbar^2}{2m_e}\sqrt{3}\gamma_2(k_x^2-k_y^2)+\dfrac{\sqrt{3}}{2}b(\varepsilon_{yy}-\varepsilon_{xx})},$$

$$\tan(\beta)=-\frac{\dfrac{\hbar^2}{m_e}\sqrt{3}\gamma_3k_xk_z-d\varepsilon_{zx}}{d\varepsilon_{yz}-\dfrac{\hbar^2}{m_e}\sqrt{3}\gamma_3k_yk_z}. \tag{9}$$

If the uniaxial stress P is applied along [110] or [100], ε_{zx} and ε_{yz} become zero, and k_z cancels out from Eq. (9). In this case, φ and η are real and the transformation is unitary. The Hamiltonian (3) transforms into

$$H'=UHU^{+}. \tag{10}$$

The values of the strain tensor components depend on the direction of the applied uniaxial compression. When the uniaxial compression P is applied along [110], the strain tensor ε_{ij} becomes

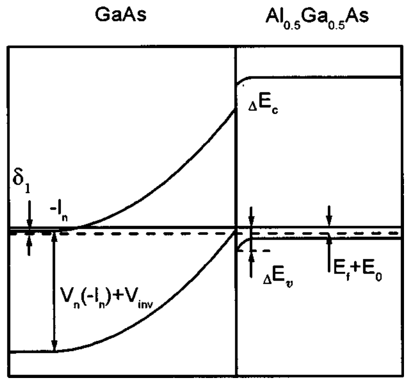

FIG. 1. Band diagram for the [001] GaAs/$Al_{0.5}Ga_{0.5}$As heterojunction.

$$\varepsilon_{xx}=\varepsilon_{yy}=(S_{11}+S_{12})\frac{P}{2},\qquad \varepsilon_{zz}=S_{12}P,\qquad \varepsilon_{xy}=S_{44}\frac{P}{4} \tag{11}$$

and for the [100] direction

$$\varepsilon_{xx}=S_{11}P,\qquad \varepsilon_{yy}=\varepsilon_{zz}=S_{12}P,\qquad \varepsilon_{xy}=0. \tag{12}$$

Here, S_{ij} are the compliance constants, and P is negative as we consider compression. After the unitary transformation the Hamiltonian (3) can be written as

$$H'=\begin{bmatrix} P+Q & A & 0 & 0\\ A^* & P-Q & 0 & 0\\ 0 & 0 & P-Q & A\\ 0 & 0 & A^* & P+Q\end{bmatrix}, \tag{13}$$

where

$$A=|R|-i\frac{\sqrt{3}\hbar^2}{m_e}\gamma_3\sqrt{(k_x^2+k_y^2)}k_z. \tag{14}$$

We chose the z direction to be perpendicular to the heterointerface. A self-consistent potential $V(z)$ is added along the diagonal and k_z is replaced by the operator $(1/i)\partial/\partial z$. So finally we numerically solve the equation

$$[H'+V(z)]\Psi=E\Psi, \tag{15}$$

where Ψ and E are the eigenfunction and corresponding eigenvalue. The potential $V(z)$ for a triangular well in the Hartree approximation consists of two terms

$$V(z)=V(z)_{dep}+V(z)_{inv}, \tag{16}$$

where $V(z)_{dep}$ is the potential formed by fixed charges in the depletion layer and $V(z)_{inv}$ is the potential created by the 2D holes in the inversion layer. $V(z)_{dep}$ is calculated in the depletion-layer approximation, i.e., it is assumed that all acceptors, with concentration N_a, in the $Al_{0.5}Ga_{0.5}$As are ion-

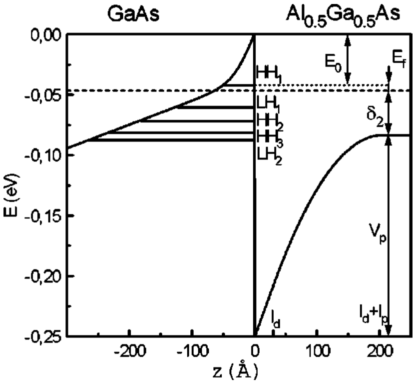

FIG. 2. Valence-band edge for the [001] GaAs/$Al_{0.5}Ga_{0.5}As$ heterojunction with the first five energy levels at $k_{\parallel}=0$ ($N_s=7.6\times10^{11}$ cm^{-2}).

ized for $l_d<z<l_d+l_p$, and that all donors, with concentration N_d, in the GaAs are ionized for $-l_n<z<0$, where the heterojunction is at $z=0$ (Figs. 1 and 2). The total concentration of 2D holes N_s in the inversion layer and the depletion layer widths l_p and l_n are determined from the following equations[4,13]

$$V_p+\delta_2+E_f+E_0={}_{\Delta}E_v, \tag{17}$$

$$V_n=E_g-\delta_1-V_{inv}(-\infty)+E_f+E_0, \tag{18}$$

$$N_a l_p=N_d l_n+N_s, \tag{19}$$

where

$$V_n=\frac{2\pi e^2}{\epsilon_1}N_d l_n^2 \tag{20}$$

and

$$V_p=\frac{2\pi e^2}{\epsilon_2}N_a l_p^2+\frac{4\pi e^2}{\epsilon_2}N_a l_p l_d. \tag{21}$$

Here, ϵ_1 and ϵ_2 are the dielectric constants of the GaAs and $Al_{0.5}Ga_{0.5}As$, δ_1 and δ_2 are the energy differences between the Fermi level and the bottom of the conduction band in the GaAs and the top of the valence band in the $Al_{0.5}Ga_{0.5}As$, respectively. The thickness of the undoped $Al_{0.5}Ga_{0.5}As$ layer is denoted by l_d and the valence-band offset by ${}_{\Delta}E_v$ (Figs. 1 and 2). E_g is the energy gap in GaAs, E_0 is the first energy level referred to the valence-band top at the heterointerface, and E_f is the Fermi energy referred to the first energy level. The Hartree potential $V_{inv}(z)$ is determined by solving Poisson's equation numerically to self-consistency

$$\frac{\partial^2 V_{inv}}{\partial z^2}=\frac{4\pi e^2}{\epsilon}\sum_{k_x,k_y}|\Psi_{k_x k_y}(z)|^2 \tag{22}$$

taking $\Psi(z)$ from Eq. (15) in each iteration.

TABLE I. Parameters used in the calculation.

		GaAs	$Al_{0.5}Ga_{0.5}As$
Luttinger parameters [a]	γ_1	6.85	5.15
	γ_2	2.1	1.39
	γ_3	2.9	2.095
Deformation potentials (eV)	a_v	-1.6 [b]	
	b	-1.7 [c]	
	d	-4.55 [c]	
Compliance constants [d] (10^{-3} kbar^{-1})	S_{11}	1.17	1.185
	S_{12}	-0.37	-0.38
	S_{44}	1.68	1.69
Dielectric constants	ϵ	12.56 [e]	11.06 [f]
Energy separation (meV)	δ	$\delta_1=6$ [e]	$\delta_2=35$ [g]

[a] Reference 4.
[b] Reference 24.
[c] Reference 25.
[d] Reference 26.
[e] Reference 27.
[f] Reference 28.
[g] Reference 29.

The values of the parameters used in the calculation are presented in the Table I. ${}_{\Delta}E_v$ is taken from the recent experimental results to be 250 meV.[14,15] The concentration of donors N_d is taken to be 1×10^{15} cm^{-3} and the concentration of acceptors N_a to be 5×10^{17} cm^{-3}. The value of the undoped layer l_d is chosen to be 30 Å in order to account for the experimentally observed hole concentration. This value is smaller than the thickness of the spacer in the wafers under investigation (70 Å). The difference may be caused by diffusion of Be from the doped layer into the spacer during wafer growths. The effect of image potential is neglected due to the small difference between the dielectric constants of GaAs and $Al_{0.5}Ga_{0.5}As$ (Table I). All calculations have been performed using the finite-difference method. This method allows to obtain an exact numerical solution of the Hamiltonian. Eigenvalues were found for different values of the quasi-wave vector k_x, k_y and of the applied uniaxial compression P.

The Fermi energy of the system is determined from the requirement that the number of available states within the areas enclosed by the two surfaces at the Fermi level (S_0 and S_1), corresponding to the two spin subbands, must be equal to the total hole concentration

$$n_0=\frac{1}{4\pi^2}S_0(E_f),\quad n_1=\frac{1}{4\pi^2}S_1(E_f),$$

$$n_0+n_1=N_s. \tag{23}$$

III. EXPERIMENT

Samples from two p-type GaAs/$Al_{0.5}Ga_{0.5}As$ wafers with single heterojunctions and hole concentrations 7.6×10^{11} cm^{-2} (HCO251) and 9.8×10^{11} cm^{-2} (HCO218) have been investigated under uniaxial compression up to 5 kbar. Only the ground-state splitted subband HH_1 (Fig. 2) is populated at these hole concentrations. The wafers were grown by molecular beam epitaxy on (001) semi-isolating

GaAs substrates. The grown layer sequences are: 1-μm undoped GaAs, 70-Å $Al_{0.5}Ga_{0.5}As$ undoped spacer, 500-Å $Al_{0.5}Ga_{0.5}As$ active layer doped with Be (1×10^{18} cm^{-3} for the HCO218 wafer and 5×10^{17} cm^{-3} for the HCO251 one), and 50-Å GaAs cap doped with Be (2×10^{18} cm^{-3} for the HCO218 wafer and 1×10^{18} cm^{-3} for the HCO251 one). The samples of the size $0.5\times0.8\times3.0$ mm^3, with the long dimension parallel to [110] or $[\bar{1}10]$ directions, were cracked from the wafers along the natural cleavage planes. Two identical Hall bar mesas, perpendicular to each other, were wet etched in the central part of the samples. We name by $S1$ the mesa with the current direction parallel to the direction of the compression, which is along the long sample dimension, and by $S2$ the perpendicular one. The samples were contacted by standard Au:Zn or Au:Mg diffusion. Linearity of the current-voltage characteristics was used as a criterion of good contact quality. Uniaxial compression was applied in the direction of the long dimension of the samples ([110] or $[\bar{1}10]$) using the technique described in Ref. 16. Magnetotransport measurements were performed in the temperature range 1.4–4.2 K and in magnetic field up to 6 T.

The samples with two mesas were aimed for a detailed investigation of anisotropy of the electrical resistance under uniaxial compression. Some results obtained on samples with only one Hall bar mesa, with current direction parallel to the uniaxial compression, have been reported previously.[17,18] The observed strong decrease of resistance in the direction of compression was ascribed to an increase of the mobility under compression. The question of stress-induced anisotropy in the 2D plane was not analyzed previously, because Shubnikov–de Haas (SdH) frequencies and Hall measurements do not allow to make conclusions concerning anisotropy of effective masses. The present measurements of the pressure dependence of the resistance in directions perpendicular and parallel to the direction of uniaxial compression can give this information.

The similarity of the two mesas $S1$ and $S2$ was controlled by SdH and Hall measurements. The difference in their carrier concentrations was found from Hall measurement to be less than 2% for all samples under investigation. The quantum Hall plateaus and the SdH peaks were observed at the same values of magnetic fields for both mesas.

The resistance of the samples at zero pressure is found to be anisotropic in the 2D plane. We ascribe this anisotropy to anisotropic roughness scattering.[19,20] It is found to depend on the sample orientation. Results of the roughness scattering anisotropy investigation will be reported separately. The lower value of resistance occurs in the $[\bar{1}10]$ direction. The ratio between resistances in the $[\bar{1}10]$ and [110] directions is 0.6–0.7. As it will be demonstrated in the present paper, the behavior of the resistance under compression is mainly determined by the direction of applied compression, being parallel or perpendicular to the transport current.

IV. RESULTS AND DISCUSSION

A. Fermi surface

The lack of inversion symmetry of the confining potential of the triangular quantum well $V(z)$ lifts the $m_j=\pm\frac{3}{2}$ degeneracy of the bulk Hamiltonian at $k_\parallel\neq0$. The importance of the symmetry $V(z)=V(-z)$—or the lack of such—may be best appreciated by noting, that change of z to $-z$ changes A to A^*, because k_z [which is $(1/i)\partial/\partial z$ and which appears in the imaginary part of A] changes to $-k_z$. In consequence, the upper-left block corresponding to Eq. (15) has the same solution as a lower-right block, i.e., the system is degenerate.

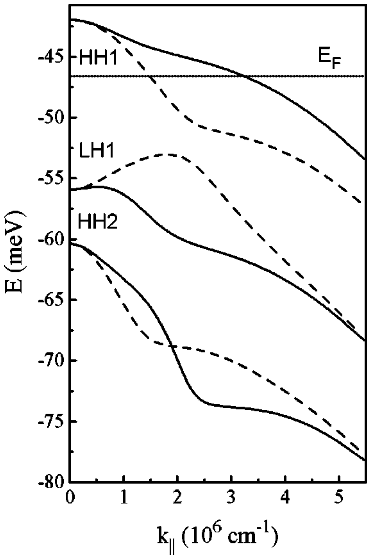

FIG. 3. Energy of the first three hole subbands in the [001] $GaAs/Al_{0.5}Ga_{0.5}As$ heterojuction ($N_s=7.6\times10^{11}$ cm^{-2}) versus $k_\parallel$ parallel to [110] direction at $P=0$. Dashed and solid lines correspond to the spin up and down states. Dotted line is the position of the Fermi level.

The first three hole subbands are shown in Fig. 3 for the structure described in Sec. II with hole concentration 7.6×10^{11} cm^{-2}. The subbands are found to depend strongly on uniaxial stress. Results for compression along [110] are plotted on Fig. 4. The Fermi level of the calculated structure ($N_s=7.6\times10^{11}$ cm^{-2}) lies 46.7 meV lower than the top of

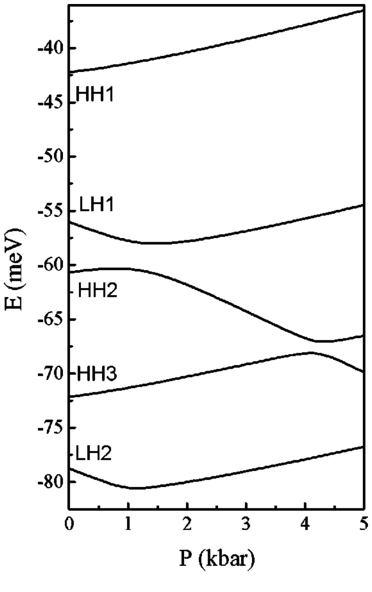

FIG. 4. Energy at $k_\parallel=0$ versus external uniaxial compression applied along [110] for the first five hole subbands.

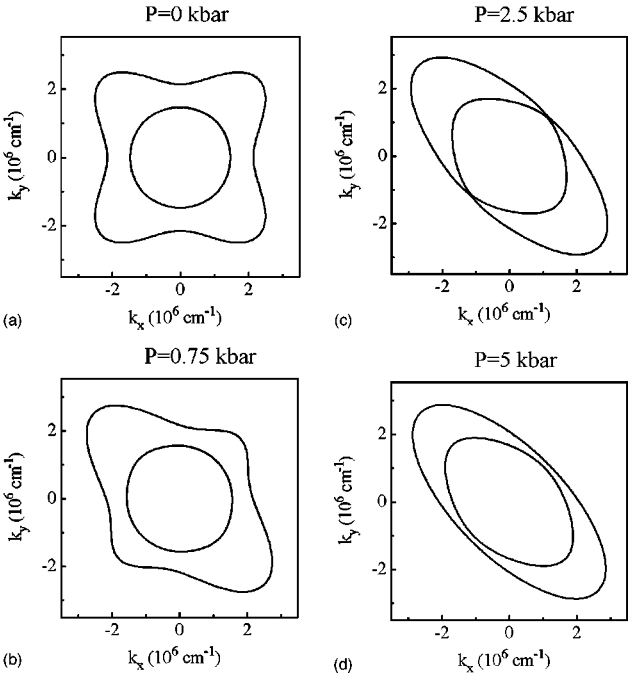

FIG. 5. Fermi surface of the two ground-state heavy-hole subbands of the p-[001] GaAs/Al$_{0.5}$Ga$_{0.5}$As heterojunction at different uniaxial compression applied along [110] direction: (a) $P=0$, (b) $P=0.75$ kbar, (c) $P=2.5$ kbar, (d) $P=5$ kbar.

the quantum well, and only the two uppermost nondegenerate hole subbands are populated (full and dotted lines of HH1 in Fig. 3).

The Fermi surfaces (FS) for different values of uniaxial compression applied in the [110] and [100] directions are presented in Figs. 5 and 6. As can be seen, the application of external uniaxial compression in the plane of the 2D system leads to strong anisotropy of the hole FS's. The FS's of the two subbands are transformed differently under compression. For the more light mass FS (the inner contour in Fig. 5) the applied compression causes a decrease of the dimension in the direction of the compression, and an increase of the dimension in the perpendicular direction. The FS corresponding to the more heavy mass is transformed in a more complicated manner. In the range from 0 to 2.5 kbar for the [110] direction, the FS dimension decreases in the direction of compression and the two FS's touch each other in two points at $P=2.5$ kbar. Further increase of the compression leads to their separation in k space and to their transformation into two approximately ellipsoidal surfaces at higher pressure (Fig. 5). A similar behavior takes place for the [100] direction of compression, but in this case the FS's touch each other at a lower value of compression (Fig. 6).

Qualitatively similar results have been obtained for the wafer with the higher carrier concentration (HCO218). In this case, the FS has a larger area in k space and the touching points are observed at higher value of compression.

The presence of touching points for the two spin-splitted subbands is caused by the two blocks of the matrix Eq. (15) having the same solutions. This occurs when $A=A^*$ or $A=-A^*$. The first case ($A=A^*$) can be fulfilled only for $k_\parallel=0$ [see Eq. (14)]. So, the touching points arise when $A=-A^*$. This may be understood by noting that the unitary transformation

$$\begin{bmatrix} 1 & 0 \\ 0 & -1 \end{bmatrix} \tag{24}$$

applied to one of the two blocks of Eq. (15), upper left or lower right, changes the sign of the off-diagonal elements, and if $A=-A^*$, then we are back at the situation when two blocks have the same solution. This means that the real part of A should be equal to zero:

$$\frac{\hbar^2\sqrt{3}}{2m_e}\gamma_2(k_x^2-k_y^2)+\frac{\sqrt{3}}{2}b(\varepsilon_{yy}-\varepsilon_{xx})=0, \tag{25}$$

$$\frac{\hbar^2\sqrt{3}}{m_e}\gamma_3 k_x k_y-d\varepsilon_{xy}=0. \tag{26}$$

When the compression is applied along [110] or [100] directions these conditions can be fulfilled, the values of the quasi-wave vector $k_\parallel$ corresponding to the touching points being obtained from Eqs. (25) and (26). For compression along [110] the result is

$$k_x=k_y=\pm\sqrt{\frac{m_e d}{\sqrt{3}\hbar^2\gamma_3}\varepsilon_{xy}} \tag{27}$$

and for the [100] direction

$$k_y=0,\quad k_x=\pm\sqrt{\frac{m_e b}{\hbar^2\gamma_2}(\varepsilon_{xx}-\varepsilon_{yy})}. \tag{28}$$

According to these equations the touching point quasi-wave vectors increase as the square root of the deformation and reach the Fermi level at a definite deformation. This situation corresponds to the touching of two hole FS's. We want to emphasize that these points, where the system has a degeneration, exist for any nonzero compression. In such points, curves of dispersion laws corresponding to the splitted subbands touch each other without crossing (Fig. 7). All subbands have their touching points at the same value of the quasi-wave vector.

B. Hole concentrations in spin-splitted subbands

At zero pressure the two subbands of the splitted ground heavy-hole state have different effective masses. We shall use indices ''0'' and ''1'' for the heavy- and light-mass subbands, respectively. The dependence of the hole concentrations n_0 and n_1 on applied compression was calculated from Eq. (23) and it is shown in Fig. 8 for compression along [110]. We find that n_0 decreases, while n_1 increases with increasing compression. This result is in qualitative agreement with our present and previous experimental data.[17,18]

The experimental carrier concentrations were calculated from SdH oscillations and Hall measurements. SdH oscillations at different pressures for a sample with $N_s=7.6\times10^{11}$ cm^{-2} are presented on Fig. 9 for the two perpendicular mesas $S1$ and $S2$. Concentrations calculated from these oscillations are shown in Fig. 10. The SdH oscillation corresponding to the higher frequency F_0 was observed only in a narrow range of magnetic fields. As regards F_S, the SdH frequency in high-magnetic fields, it corresponds to the total hole concentration. The accuracy of F_S was poor due to the

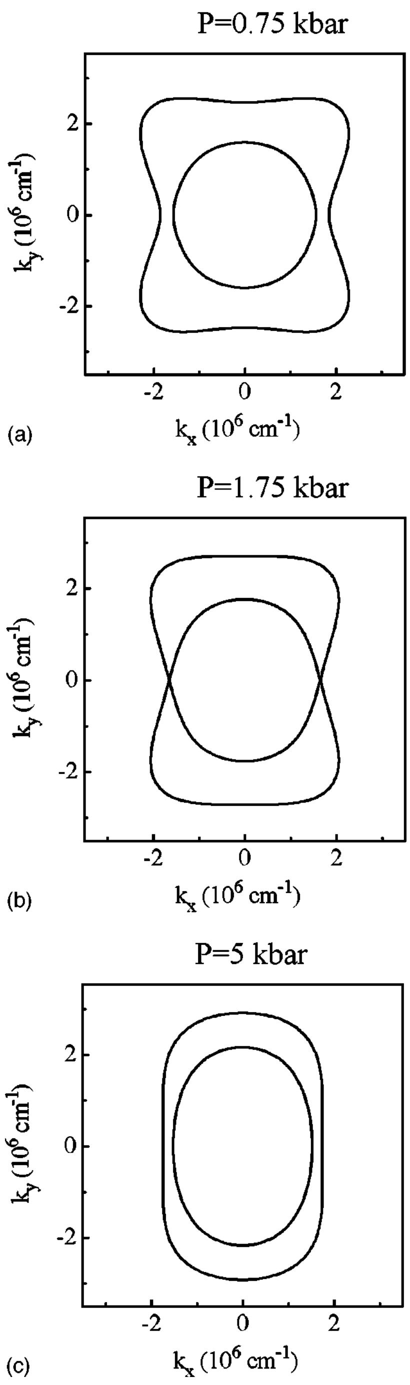

FIG. 6. Fermi surface of the two ground-state heavy-hole subbands of the p-type [001] GaAs/Al$_{0.5}$Ga$_{0.5}$As heterojunction at different uniaxial compression applied along [100] direction: (a) $P = 0.75$ kbar, (b) $P = 1.75$ kbar, (c) $P = 5$ kbar.

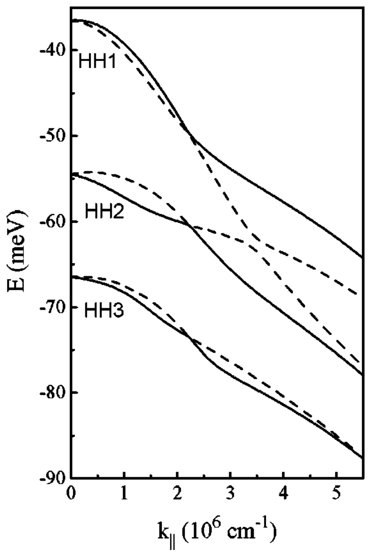

FIG. 7. Energy versus $k_{\|}$ parallel to the [110] direction for the three spin-splitted hole subbands in the [001] GaAs/Al$_{0.5}$Ga$_{0.5}$As heterojunction at an external uniaxial compression $P = 5$ kbar applied along [110]. Dashed and solid lines correspond to the spin up and down states.

limited range of magnetic fields where it was observed. The total hole concentration was calculated from Hall measurement as well. These give concentrations in agreement with those derived from the SdH oscillations. Under uniaxial compression, F_0 and F_1 shift in opposite directions, and so do the corresponding densities of nondegenerate carriers $n_i = F_i(e/h)$. The ratio n_0/n_1 between the hole concentrations in the two subbands significantly decreases under compression: from $n_0/n_1 \simeq 2$ at $P = 0$ to $n_0/n_1 \simeq 1.15$ at $P = 4.8$ kbar. At any applied compression the sum of the carrier concentrations in the subbands corresponds, within the accuracy of the measurement, to the total carrier concentration in the 2D hole system. The total carrier concentration at $P = 0$ is $N_s = 7.6 \times 10^{11}$ cm^{-2} for HCO251 and $N_s = 9.8 \times 10^{11}$ cm^{-2} for HCO218, and shows about a 3% decrease per kbar.

As can be seen from Figs. 8 and 10, there is only a qualitative agreement between the experimental and the calculated behavior of n_0/n_1 under uniaxial compression. The main difference occurs without compression: $n_0/n_1 \simeq 3$ from the calculation, while $n_0/n_1 \simeq 2$ from the experiment. Too large values of n_0/n_1 have been found also in previous calculations for similar unstrained p-type GaAs/Al$_{0.5}$Ga$_{0.5}$As heterostructures.[3,4] Variation of the input parameters N_a, N_d, l_d, ΔE_v inside reasonable ranges was not helpful in solving this problem of discrepancy. A possible reason for

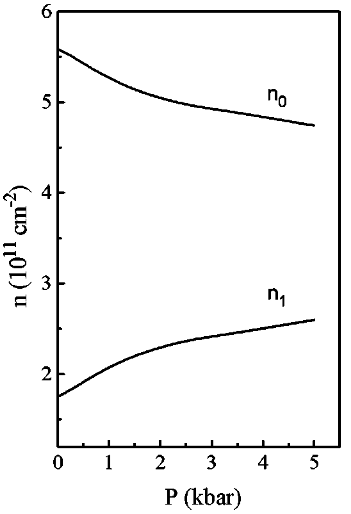

FIG. 8. Dependence of hole concentrations in spin subbands "0" and "1" in the [001] GaAs/Al$_{0.5}$Ga$_{0.5}$As heterojunction on uniaxial compression applied along the [110] direction.

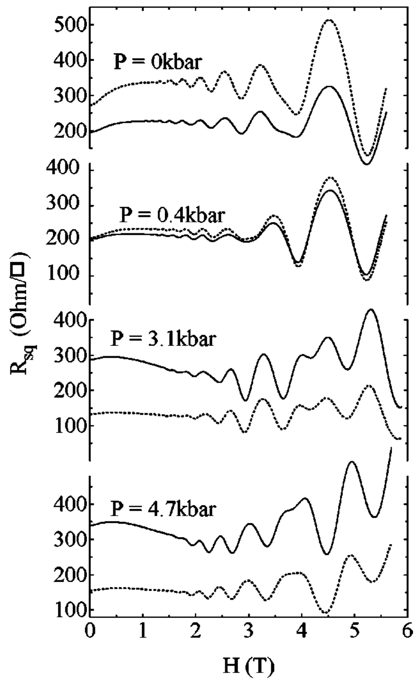

FIG. 9. SdH oscillations for a sample with carrier concentration $N_s = 7.6\times10^{11}$ cm^{-2} (HCO251) at different pressures applied along the [110] direction. Dotted lines correspond to the mesa $S1$ having the direction of current parallel to the compression, solid lines correspond to the mesa $S2$ having the direction of current perpendicular to the compression.

it might be the assumption of an abrupt potential jump at the interface. Recently, segregation of Ga at AlAs/GaAs interface has been studied, and up to 20 crystal planes were reported as segregation range for Ga.[21] Therefore, it is necessary to consider a more complicated behavior of the valence-band potential at the heterointerface to improve the numerical calculations. Till now this problem has not been studied and the way in which the valence-band potential changes at the interface is unknown. Introducing a slope of the valence-band jump would lead to a more symmetric well, and as consequently to a reduced subband splitting. Due to the absence of clear data concerning the range and the form of the potential transition we have used the simplest model, i.e., an abrupt jump.

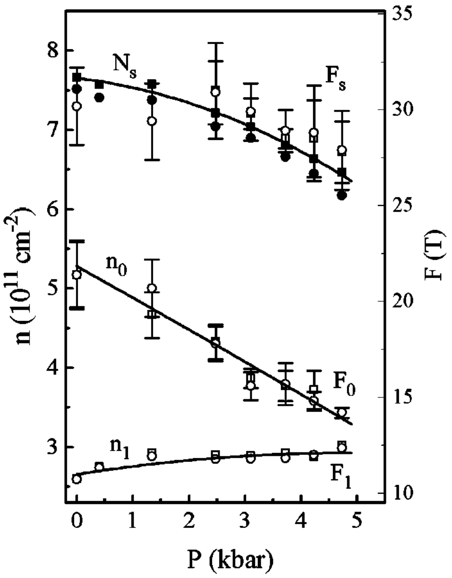

FIG. 10. Pressure dependence of the total hole concentration and of the concentrations in subbands ''0'' and ''1'' for HCO251. The compression is along [110]. Open circles and squares correspond to concentrations calculated from SdH oscillations for the two perpendicular mesas $S1$ and $S2$. Filled circles and squares correspond to the total hole concentration calculated from Hall measurements for $S1$ and $S2$ mesas, respectively.

C. Effective cyclotron masses

The experimental dependence of the cyclotron mass on uniaxial compression was calculated from the temperature dependence of SdH oscillation amplitudes (Fig. 11). Due to the considerable decrease of these with increasing temperature, the masses were calculated from the curves at 1.4 and 2.0 K. The complicated oscillation picture in high-magnetic fields and the narrow temperature range reduced the accuracy of the light-mass calculations and did not allow to estimate the mass corresponding to the heavier subband. The light mass was calculated in the lower range of magnetic fields ($H<2$–3 T), where the oscillations were observed to be dominated by a single frequency. This way of mass calculation is valid for the single-particle model and might have to be modified, as it was reported recently that strong exchange interactions in p-type GaAs/Al$_x$Ga$_{1-x}$As heterostructures play an important role and affect the temperature dependence of SdH oscillation amplitudes at temperatures below 1 K.[22] However, in our temperature range, we consider masses obtained from the single-particle model to be reliable estimates. The uncertainty in absolute mass measurement may not be that important for the considerations of the influence of pressure on the cyclotron masses. To obtain experimental mass values for comparison with our calculations, we used, as it was done previously,[1] a linear extrapolation of the magnetic-field dependence to zero magnetic field (Fig. 11). In this way, the mass at zero stress was found to be $m_1^*/m_e = (0.23\pm0.01)$ for samples with $N_s = 7.6\times10^{11}$ cm^{-2} (Fig. 12) and $m_1^*/m_e = (0.25\pm0.01)$ for samples with $N_s = 9.8\times10^{11}$ cm^{-2}. The magnetic-field coefficient in the noncompressed state is $\partial m_1^*/\partial H = 0.057 m_e/T$ for HCO251 ($\partial m_1^*/\partial H = 0.051 m_e/T$ for HCO218). These values are in a good agreement with those of Ref. 1, where similar heterostructures were investigated, but clearly different from those of Ref. 23. The reason for the difference of effective masses obtained by different authors might be the different conditions of heterostructure growth and the different layer thicknesses, which can affect the form of ''triangular well.''

In Fig. 12 we display our results for the two masses as a function of [110] compression. The theoretical values were derived from

$$m_i^* = \frac{\hbar^2}{2\pi}\left(\frac{\partial S_i}{\partial E}\right)_{E_f}, \quad i=0,1, \tag{29}$$

where S_i is the area in k space enclosed by the Fermi surface for each of the spin subbands. The experimental zero-field hole mass m_1^*/m_e increases under uniaxial compression as does the theoretical one.

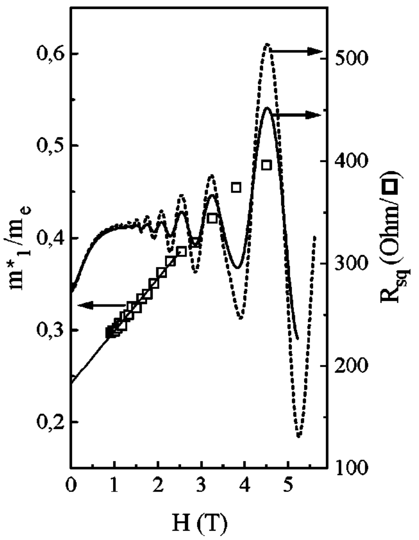

FIG. 11. SdH oscillations (right scale) for HCO251 at two different temperatures $(P=0):T=1.97$ K (solid line), $T=1.44$ K (dashed line). Effective mass (left scale) for subband "1" (open squares) calculated from the temperature dependence of the SdH oscillations. The straight line is a linear approximation of the effective mass magnetic-field dependence.

The samples with higher hole concentration (and according to the theoretical prediction with a higher splitting and a larger difference of masses) demonstrate a larger increase of m_1^* under compression.

The results for the hole concentrations (Sec. IV B) and for the masses reveal both of them a decrease of the splitting under compression and a redistribution of carriers between the two subbands in favor of the less populated one. The dependence of the effective mass on magnetic field decreases under compression from $\partial m_1^*/\partial H=(0.057\pm0.004)m_e/T$ at $P=0$ to $(0.004\pm0.005)m_e/T$ at $P=4.8$ kbar. It disappears at pressures higher than 4 kbar, which we ascribe to a reduction of the difference between the subbands.

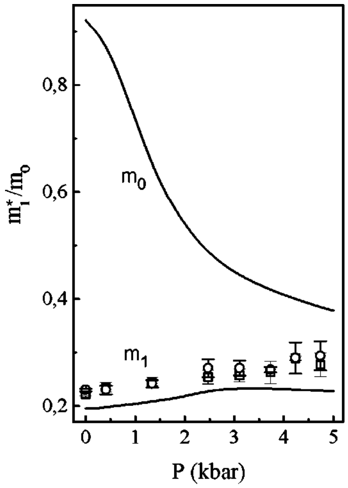

FIG. 12. Dependence of effective masses in spin-splitted subbands on external uniaxial compression applied along [110]. Solid lines correspond to calculated values of effective masses. Circles and squares are experimental values for two perpendicular mesas for HCO251 sample.

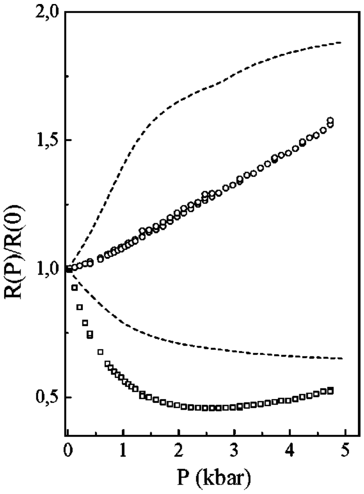

FIG. 13. Dependence of the relative resistance in two perpendicular directions on external [110] uniaxial compression. Squares and circles are experimental data for the directions of transport current parallel and perpendicular to the compression, respectively (HCO251), dash lines are result of calculations.

D. Electrical resistance

The pressure dependence of the electrical resistance was calculated for the directions of the transport current being parallel or perpendicular to the direction of compression. We assumed the dependence to arise solely from band-structure effects, i.e., we neglected any influence from a possible pressure dependence of the scattering processes, and simply described the scattering by constant isotropic mean-free path λ. Thus, the conductivity was calculated from the kinetic equation

$$\vec{j}=-\frac{e^2}{4\pi^2}\int(\vec{E}\vec{V})\vec{V}\frac{\lambda}{|V|}\frac{\partial f_0}{\partial E}dk_x dk_y, \tag{30}$$

where $\vec{j}$ is the current density, $\vec{E}$ is the electric field, $\vec{V}$ the velocity of the carriers, and f_0 the distribution function.

The results for a sample with carrier concentration $N_s=7.6\times10^{11}\ \mathrm{cm}^{-2}$ under [110] compressive strain are shown in Fig. 13 (dash line), where we have divided the resistance at pressure P by the resistance at zero pressure. By this way of displaying we avoid to account for the anisotropy of $R(P=0)$, cf. Sec. III, an anisotropy, which by the assumption of an isotropic λ was neglected in the calculations. Under uniaxial compression the square resistance of the samples demonstrates considerable change of its anisotropy: in the direction parallel to the external uniaxial compression it decreases while it increases in the perpendicular direction. The experimental results are qualitatively the same for both directions of compression [110] and $[\bar{1}10]$. Slight differences we ascribed to the roughness scattering. Naturally, this scattering mechanism as well others and their pressure dependence should be taken into account in a more realistic analysis of resistance under uniaxial compression. However, our calculations indicate that the evolution of the hole FS is a main cause determining the behavior of the resistance under compression.

V. CONCLUSION

The effect of uniaxial compression on the electronic structure and the magnetotransport properties of triangular quantum wells has been investigated theoretically and experimentally. It has been found that uniaxial compression strongly affects the Fermi-surface topology, leading to a reduction of the difference between the effective masses and the carrier concentrations in the subbands of the hole ground state. It also causes a strong anisotropy of the electrical resistance in the directions parallel and perpendicular to the direction of the applied compression.

ACKNOWLEDGMENTS

This work was supported by ''Carlsbergfondet'' Grant No. 970300/10-1195, Grant No. 9601512 from the Danish Research Council, and Russian Foundation for Basic Research Grant No. 97-02-17685. For wafer growths and sample preparation we acknowledge the work of Claus B. Sorensen.

---

[1] J. P. Eisenstein, H. L. Störmer, V. Narayanamurti, A. C. Gossard, and W. Wiegmann, Phys. Rev. Lett. **53**, 2579 (1984).

[2] H. L. Störmer, Z. Schlesinger, A. Chang, D. C. Tsui, A. C. Gossard, and W. Wiegmann, Phys. Rev. Lett. **51**, 126 (1983).

[3] E. Bangert and G. Landwehr, Superlattices Microstruct. **1**, 363 (1985).

[4] U. Ekenberg and M. Altarelli, Phys. Rev. B **32**, 3712 (1985).

[5] D. A. Broido and L. J. Sham, Phys. Rev. B **31**, 888 (1985).

[6] O. Mauritz and U. Ekenberg, Phys. Rev. B **55**, 10 729 (1997).

[7] M. Silver, W. Batty, A. Ghiti, and E. P. O'Reilly, Phys. Rev. B **46**, 6781 (1992).

[8] G. Platero and M. Altarelli, Phys. Rev. B **36**, 6591 (1987).

[9] J. Lee and M. O. Vassell, Phys. Rev. B **37**, 8855 (1988).

[10] J. Los, A. Fasolino, and A. Catellani, Phys. Rev. B **53**, 4630 (1996).

[11] J. M. Luttinger and W. Kohn, Phys. Rev. **97**, 869 (1955).

[12] G. L. Bir and G. E. Pikus, *Symmetry and Strain-Induced Effects in Semiconductors* (Wiley, New York, 1974).

[13] T. C. Hsieh, K. Hess, J. J. Coleman, and P. D. Dapkus, Solid-State Electron. **26**, 1173 (1983).

[14] T. Forchhammer, E. Veje, and P. Tidemand-Petersson, Phys. Rev. B **52**, 14 693 (1995).

[15] M. Missous, in *Properties of Aluminum Gallium Arsenide*, edited by S. Adachi, EMIS Datareview Series No. 7 (INSPEC, London, 1993), p. 73.

[16] N. B. Brandt, V. S. Egorov, M. Yu. Lavrenyuk, N. Ya. Minina, and A. M. Savin, Zh. Éksp. Teor. Fiz. **89**, 2257 (1985) [Sov. Phys. JETP **62**, 1303 (1985)].

[17] O. P. Hansen, J. S. Olsen, W. Kraak, B. Saffian, N. Ya. Minina, and A. M. Savin, Phys. Rev. B **54**, 1533 (1996).

[18] O. P. Hansen, W. Kraak, N. Minina, J. S. Olsen, B. Saffian, and A. M. Savin, Phys. Status Solidi B **198**, 295 (1996).

[19] Y. Markus, U. Meirav, Hadas Shtrikman, and B. Laiktman, Semicond. Sci. Technol. **9**, 1297 (1994).

[20] T. Schweizer, K. Köhler, W. Rothemund, and P. Ganser, Appl. Phys. Lett. **59**, 2736 (1991).

[21] W. Braun, A. Trampert, L. Däweritz, and K. H. Ploog, Phys. Rev. B **55**, 1689 (1997).

[22] M. Kemerink, P. M. Koenraad, and J. H. Wolter, Phys. Rev. B **57**, 6629 (1998).

[23] E. Mendez, Surf. Sci. **170**, 561 (1986).

[24] M. Cardona and N. E. Christensen, Phys. Rev. B **35**, 6182 (1987).

[25] F. H. Pollak, in *Properties of Aluminum Gallium Arsenide* (Ref. 15), p. 78.

[26] S. Adachi, in *Properties of Aluminum Gallium Arsenide* (Ref. 15), p. 17.

[27] G. E. Stillman, D. M. Larsen, C. M. Wolfe, and R. C. Brandt, Solid State Commun. **9**, 2245 (1971).

[28] H. C. Casey, Jr. and M. B. Panish, *Heterostructure Laser, Part A. Fundamental Principles* (Academic, New York, 1978).

[29] H. L. Störmer and W. T. Tsang, Appl. Phys. Lett. **36**, 685 (1980).